RESEARCH ARTICLE

Check for updates

Chemical conversion of metal–organic frameworks into hemi-covalent organic frameworks†

Xinxin Wang,‡[a] Ganggang Chang, [ID] ‡[b] Chenxi Liu,[a] Ruidong Li,[b] Yucheng Jin,[a] Xu Ding,[a] Xiaolin Liu,[a] Hailong Wang, [ID] *[a] Tianyu Wang [ID] *[a] and Jianzhuang Jiang [ID] *[a]

Metal–organic frameworks (MOFs) and covalent organic frameworks (COFs) represent two dominant kinds of reticular materials. Mutual chemical conversion of these two species, however, still remains unreported. Herein, the reaction of a two-dimensional MOF, $Ni_3(HITP)_2$ (HITP = 2,3,6,7,10,11-hexaiminotriphenylene), with 1,1,3,3-tetramethoxypropane induces the cyclization transformation of partial bis(diimine) nickel coordination subunits to tetraaza[14]annulene (TAA) metallomacrocycle moieties. A hemi-covalent organic framework, P-$Ni_3(TAA)_3$, with different conversion efficiencies (P) of 34–72% for bis(diimine) nickel units depending on the reaction time has been obtained and preserves permanent porosity and crystallinity. The corresponding time-dependent conversion has been assessed by FT-IR spectroscopy, XPS, SEM, TEM, and powder X-ray diffraction analyses. In comparison with $Ni_3(HITP)_2$, 40%-$Ni_3(TAA)_3$ exhibits improved chemical stability under acidic conditions and significantly enhanced catalytic properties towards the photocatalytic CO_2 reduction. This result will be surely helpful in mutual investigations covering both MOFs and COFs.

1. Introduction

Metal–organic frameworks (MOFs) have been constructed by the periodically ordered assembly between molecular organic linkers and metal ions/clusters through coordination interactions.[1–10] Covalent organic frameworks (COFs) are another kind of crystalline porous molecule-based material fabricated from organic spacers by covalent bonds.[11–23] Fundamentally, MOFs should have more versatile functionalities in comparison with COFs due to their hybridization nature of metal ions and organic linkers. However, their relatively poor stability associated with the weaker strength of coordination bonds relative to covalent bonds retards their practical applications to quite a large degree. It is worth noting that metal ions in porous MOFs have been found to play an important role in many applications including gas adsorption and separation,[24–27] catalysis,[28–32] and chemical sensing.[33,34] As a consequence, the integration of MOF and COF comple-

mentarity to create metal-containing COFs (MCOFs), through either the introduction of metal complexes as building blocks or the formation of metal-coordinating molecular subunits during the assembly as well as the post-synthetic modification (PSM) processes, should be able to further expand COF functionalities.[35–37] However, despite the reports of many interesting MCOFs with outstanding properties,[35–45] the study of their chemistry is still at the infancy stage. On the one hand, few metal complexes have been used as building blocks in the direct synthesis of MCOFs.[35,46,47] On the other hand, in comparison with metal free molecules, the employment of some metal complexes such as porphyrin leads to only poorly crystalline and amorphous materials.[48,49] New approaches towards designing and fabricating MCOFs are therefore highly desired for the purpose of affording more functional reticular materials.

In addition to the predesign and synthetic strategy, the PSM concept has been demonstrated to open a new avenue to alter the physical and chemical properties of MOFs, without changing their intrinsic porous property.[50–53] According to the category of formed/broken chemical bonds, PSM approaches have been classified as (i) covalent PSM, (ii) coordinate PSM, and (iii) post-synthetic deprotection (PSD).[53] In contrast to the other two methods, covalent PSM is able to introduce versatile chemical groups onto linkers depending on flexible heterogeneous organic reactions performed on MOFs, providing inaccessible functional reticular materials beyond the direct synthesis.[53] To the best of our knowledge, covalent PSM around metal nodes of MOFs to simultaneously change

[a]*Beijing Key Laboratory for Science and Application of Functional Molecular and Crystalline Materials, Department of Chemistry, School of Chemistry and Biological Engineering, University of Science and Technology Beijing, Beijing 100083, China. E-mail: hlwang@ustb.edu.cn, twang@ustb.edu.cn, jianzhuang@ustb.edu.cn*
[b]*School of Chemistry, Chemical Engineering and Life Science, Wuhan University of Technology, 122, Luoshi Road, 430070 Wuhan, Hubei, China*
†Electronic supplementary information (ESI) available: Experimental section and additional figures and tables. See DOI: https://doi.org/10.1039/d2qi01234k
‡These authors contributed equally to this work.

metastable coordination linkages and metallic activity has not yet been explored due to the lack of suitable materials for post-synthetic covalent reactions. Herein, a covalent PSM example that simultaneously modifies the coordination connections and catalytic sites of MOFs towards preparing MCOFs has been introduced.

In detail, a porous two-dimensional (2D) MOF, [Ni$_3$(HITP)$_2$] (HITP = 2,3,6,7,10,11-hexaiminotriphenylene), has been selected as the candidate for covalent PSM. In this MOF, partial bis(diimine) nickel subunits react with 1,1,3,3-tetra-methoxypropane (TMP) to generate tetraaza[14]annulene (TAA) metallomacrocycles, resulting in the isolation of a hemi-COF P-Ni$_3$(TAA)$_3$ (P represents the conversion efficiency of bis(diimine) nickel units) containing both coordination and covalent linkages. Such a transformation has been investigated by Fourier transform infrared (FT-IR) spectroscopy, X-ray photoelectron spectroscopy (XPS), scanning electron microscopy (SEM), transmission electron microscopy (TEM), powder X-ray diffraction (PXRD), and gas sorption experiments. In comparison with Ni$_3$(HITP)$_2$, the optimal hemi-COF 40%-Ni$_3$(TAA)$_3$ obtained from 12 hours cyclization reaction shows improved chemical stability and catalytic properties, as indicated by the solution resistance under acidic conditions (pH = 1) and the photocatalytic CO$_2$ production rate under the same conditions, respectively.

2.   Experimental

All reagents were commercially available and directly employed. 4HNi and Ni$_3$(HITP)$_2$ were prepared according to the reported methods.[54–56]

Synthesis of tetraaza[14]annulene nickel Ni(TAA)

A mixture of 4HNi (100.0 mg, 0.37 mmol), N,N-dimethyl-formamide (DMF, 9.0 mL), H$_2$O (6.0 mL), triethylamine (Et$_3$N, 250.0 μL), and TMP (200.0 μL) was heated to reflux under N$_2$ for 12 h. The reaction mixture was then cooled to room temperature, filtered, and washed with water (3 × 20.0 mL), giving Ni(TAA) (90.0 mg, 71%) as a reddish brown solid. ^{1}H NMR (400 MHz, CDCl$_3$): δ (ppm) 7.68 (d, 4H), 7.67(d, 4H), 6.86 (d, 4H), 5.40 (d, 2H). MALDI-TOF MS calculated m/z = 344.1 for [M]$^+$, measured m/z = 344.4.

Synthesis of P-Ni$_3$(TAA)$_3$

Ni$_3$(HITP)$_2$ (20.0 mg) and 1,1,3,3-tetramethoxypropane (40.0 μL) were added to a mixed solution of DMF/H$_2$O (3.0 mL, v : v = 3 : 2) in a Pyrex tube. After the addition of Et$_3$N (50.0 μL), the mixture was sonicated to form a homogeneous dispersion, which was degassed by three freeze–pump–thaw cycles. The tube was flame-sealed and heated at 140 °C for 6, 12, 18, 24 and 30 hours, giving 34%-Ni$_3$(TAA)$_3$, 40%-Ni$_3$(TAA)$_3$, 55%-Ni$_3$(TAA)$_3$, 63%-Ni$_3$(TAA)$_3$, and 72%-Ni$_3$(TAA)$_3$, respectively. The precipitated solid was collected by filtration and washed with water (3 × 20.0 mL) and a small amount of methanol (5.0 mL). The obtained solid was then dried under vacuum at 100 °C.

3.   Results and discussion

Syntheses

For the purpose of obtaining COFs from MOFs through covalent PSM, we firstly investigated the Cambridge Structural
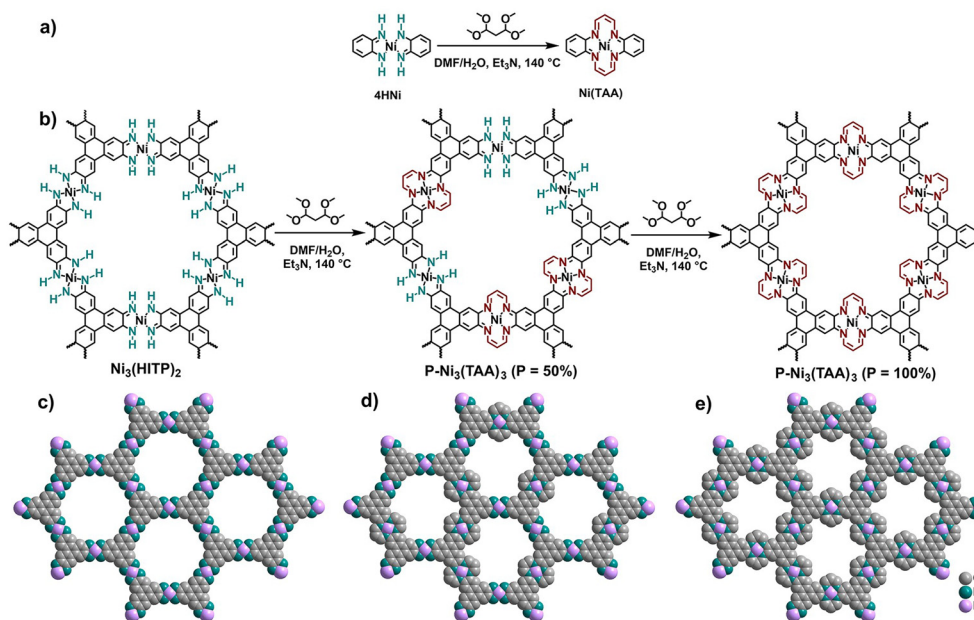
Scheme 1 (a) PSM model reaction for the preparation of Ni(TAA) from 4HNi. (b) PSM of Ni$_3$(HITP)$_2$ for the preparation of the proposed hemi-COF P-Ni$_3$(TAA)$_3$ (P = 50 and 100% represents the conversion efficiency for bis(diimine) nickel units; in the present case, only 34–72% bis(diimine) nickel units were able to be transformed). (c, d and e) Packing structures of the proposed Ni$_3$(HITP)$_2$, 50%-Ni$_3$(TAA)$_3$ and 100%-Ni$_3$(TAA)$_3$, respectively.

Database to search for promising metallomacrocycles. The tetra-aza[14]annulene (TAA) metallomacrocycle therefore attracted our attention since it has been demonstrated to serve as the covalent linkage in the assembly of MCOFs.[57,58] Fortunately, a 2D versatile MOF, $Ni_3(HITP)_2$ possessing bis(diimine) nickel subunits as coordination nodes, was previously reported.[57] It is reasonable to envision the transformation of $Ni_3(HITP)_2$ to $Ni_3(TAA)_3$ through chemical conversion of a bis(diimine) nickel subunit into a TAA metallomacrocycle moiety, Scheme 1. Before the chemical PSM for $Ni_3(HITP)_2$, a mononuclear bis(diimine) nickel compound (4HNi) was firstly synthesized using a reported method,[54] Fig. S1.† The PSM model reaction of 4HNi with TMP in the presence of Et_3N was then attempted, leading to the successful generation of Ni(TAA) under different conditions, Fig. S2 and S3.† The reaction of 4HNi and TMP in a molar ratio of 1 : 4 in DMF/H_2O ($v : v = 3 : 2$) at reflux for 6 hours was identified as the most optimized condition, giving Ni(TAA) in a yield of 71%, Fig. S4 and S5.† Such reaction conditions were therefore employed in the solvothermal reaction of $Ni_3(HITP)_2$ for

covalent PSM, affording a series of $P\text{-}Ni_3(TAA)_3$ with the conversion efficiency of $P = 34–72\%$ for bis(diimine) nickel units depending on the reaction time from 6 to 30 hours. The conversion efficiency was deduced according to XPS results mentioned later. Further prolonging the reaction time did not induce an increase of the conversion efficiency of bis(diimine) nickel subunits from $Ni_3(HITP)_2$. In other words, 100%-$Ni_3(TAA)_3$ could not be isolated by this covalent PSM method even if the reaction time prolonged to several days. This result is in line with the isolation of $Ni_3(TAA)_2$ possessing a conversion efficiency of the bis(diimine) nickel subunit of less than 100% from the direct reaction between the HITP·6HCl and TMP building blocks in the presence of nickel ions.[57]

Characterization

Due to the best photocatalytic performance of 40%-$Ni_3(TAA)_3$ as detailed below, this sample is selected as the representative for characteristic description. As shown in the FT-IR spectrum of $Ni_3(HITP)_2$, Fig. 1i, a characteristic N–H stretching band
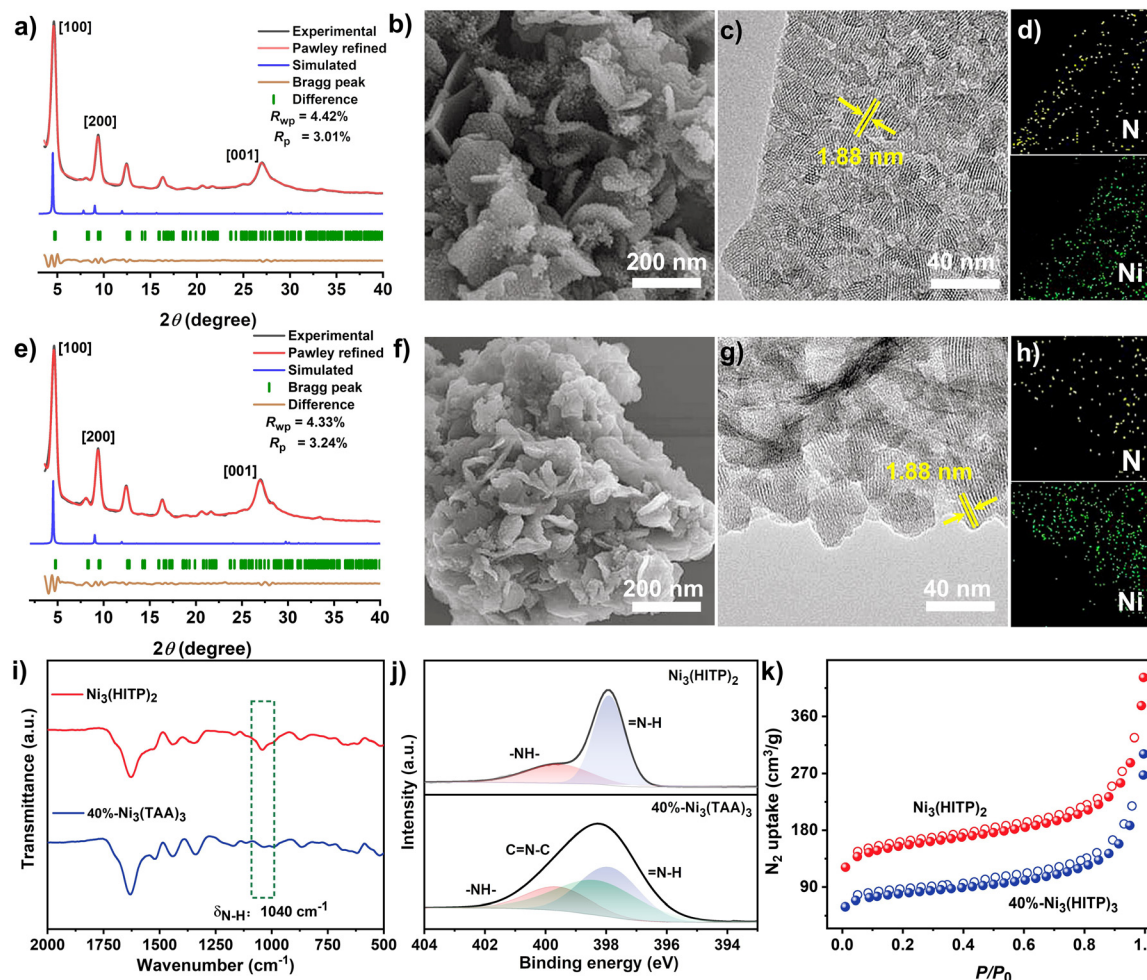

Fig. 1 PXRD patterns of $Ni_3(HITP)_2$ (a) and 40%-$Ni_3(TAA)_3$ (e): experimental PXRD profile (black), refined profile (red), difference (orange), and simulation pattern based on the AA stacking manner (blue). SEM, HRTEM, and EDS mapping photographs of $Ni_3(HITP)_2$ (b–d) and 40%-$Ni_3(TAA)_3$ (f–h). (i) FT-IR spectra of $Ni_3(HITP)_2$ and 40%-$Ni_3(TAA)_3$. (j) N 1s XPS spectra of $Ni_3(HITP)_2$ and 40%-$Ni_3(TAA)_3$. (k) Comparison of N_2 sorption isotherms for the materials $Ni_3(HITP)_2$ and 40%-$Ni_3(TAA)_3$. Solid and open circles represent the adsorption and desorption branches, respectively.

appears at 1040 cm^{-1},[59] which significantly weakens in the FT-IR spectrum of 40%-Ni$_3$(TAA)$_3$. Observation of the peaks at 2θ = 4.7°, 9.4°, 12.5°, and 16.5° in the PXRD pattern of Ni$_3$(HITP)$_2$ indexed to (100), (200), (310), and (004) reflections, respectively, confirms the single phase of this MOF. According to the PXRD analysis of 40%-Ni$_3$(TAA)$_3$ in Fig. 1a, it still remains in the crystalline phase. Nevertheless, a comparison of the PXRD patterns between Ni$_3$(HITP)$_2$ and 40%-Ni$_3$(TAA)$_3$ indicates their similar crystalline phases due to the chemical conversion occurring on coordination linkages of only a part (40%) of the bis(diimine) nickel units in the MOF, Fig. 1a and e. At the end of this paragraph, it is noteworthy that the present result suggests the most possible step-wise formation process of previously reported Ni$_3$(TAA)$_3$ from the one-pot reaction among nickel ions, TMP, and HITP,[57] namely firstly forming bis(diimine) nickel subunits as coordination linkages of the MOF and then partially converting them into the metallomacrocycles.

SEM and TEM photographs reveal that both Ni$_3$(HITP)$_2$ and 40%-Ni$_3$(TAA)$_3$ exhibit an irregular thin nanosheet morphology, Fig. 1b and f. The clear lattice stripes with a distance of ~1.9 nm over these two samples in TEM photographs are assigned to (100) reflection, Fig. 1g, further disclosing their good crystallinity. The mapping diagrams of Ni$_3$(HITP)$_2$ and 40%-Ni$_3$(TAA)$_3$ disclose the uniform distribution of Ni and N elements, Fig. 1d and h. Moreover, Ni$_3$(HITP)$_2$ becomes amorphous after immersion in 1 M HCl for 3 hours according to the PXRD pattern in Fig. S12.† In good contrast, 40%-Ni$_3$(TAA)$_3$ still possesses the crystallinity under the same conditions, indicating its enhanced chemical stability associated with the covalent PSM of coordination linkages of the MOF.

The N 1s XPS spectrum of 4HNi displays two peaks at 399.6 and 397.9 eV, Fig. S7,† which are assigned to the anilinic amine (–NH–) and quinoid imine (=NH–), respectively. In contrast, the pure monomeric compound Ni(TAA) exhibits a broad band at 398.3 eV due to the sole imine (=N–) nitrogen atoms. The XPS N 1s spectrum of Ni$_3$(HITP)$_2$ shows two peaks at 399.6 and 397.9 eV, which are attributed to the anilinic amine (–NH–) and quinoid imine (=NH–), in good agreement with the abovementioned model compound 4HNi, Fig. S9.† After PSM, only a broad band at 397.9 eV is observed for the hemi-COF 40%-Ni$_3$(TAA)$_3$. Although the XPS N 1s spectrum of 40%-Ni$_3$(TAA)$_3$ is overall similar to that for the pure Ni(TAA) compound, its broad band can be deconvoluted into three peaks at 399.6, 397.9, and 398.3 eV (Fig. S10†) due to the presence of anilinic amine (–NH–), quinoid imine (=NH–), and imine (=N–) nitrogen atoms. A comparative study of the integral area
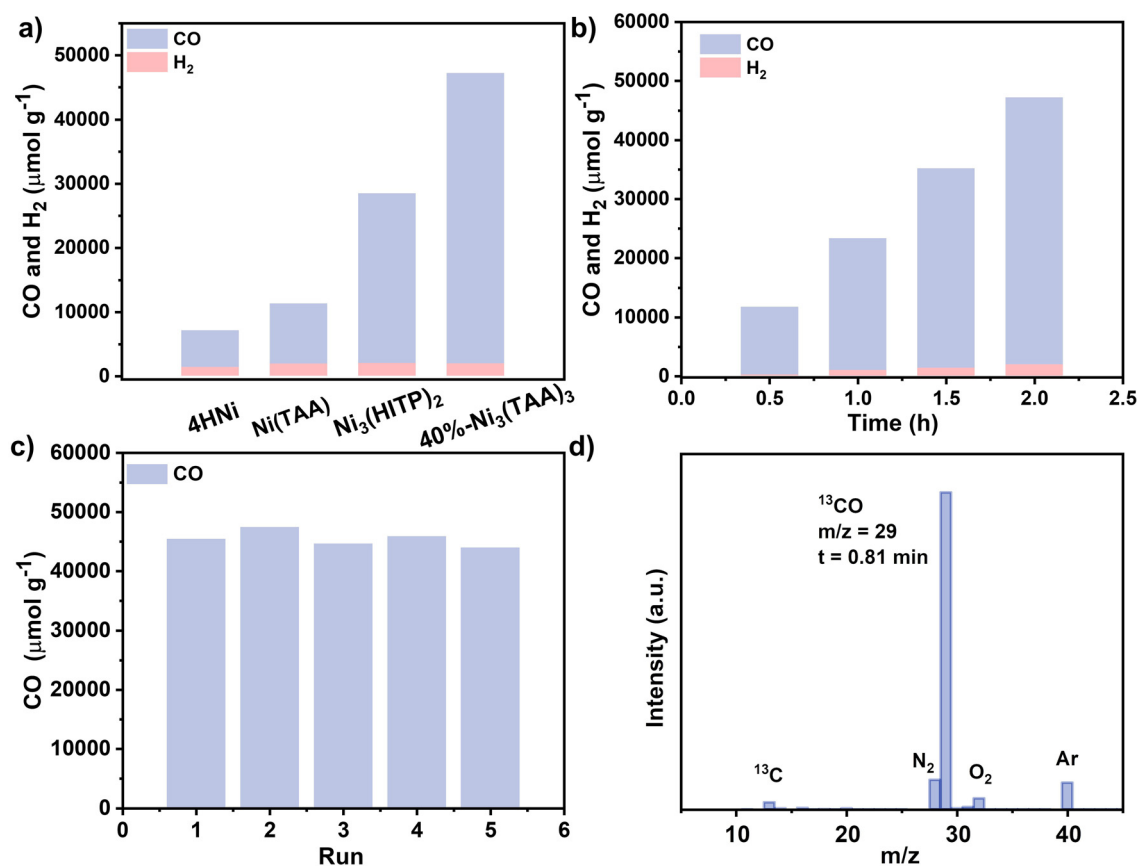
Fig. 2 (a) Comparison of the CO$_2$RR performance of 40%-Ni$_3$(TAA)$_3$ with those of Ni$_3$(HITP)$_2$, 4HNi, and Ni(TAA). (b) Time-dependent CO production performance using 40%-Ni$_3$(TAA)$_3$ as the photocatalyst. (c) Durability tests of 40%-Ni$_3$(TAA)$_3$. (d) Mass spectra of the products of photocatalytic CO$_2$ reduction by using ^{13}CO$_2$.

This journal is © the Partner Organisations 2022

Inorg. Chem. Front., 2022, 9, 4776–4784 | 4779

of –NH–/═NH– and ═N– signals for 40%-Ni$_3$(TAA)$_3$ quantitatively shows a conversion efficiency of 40%, revealing that its chemical structure contained both bis(diimine) nickel subunits and tetraaza[14]annulene metallomacrocycles.

This demonstrates the hemi-COF nature of 40%-Ni$_3$(TAA)$_3$, as an intermediate between an MOF and a COF.

Nitrogen sorption isotherms of 40%-Ni$_3$(TAA)$_3$ together with the other four *P*-Ni$_3$(TAA)$_3$ (*P* = 34, 55, 63, and 72%) were recorded at 77 K, Fig. S10.† The degassed samples exhibit type I sorption behaviors. The Brunauer–Emmett–Teller (BET) surface areas of *P*-Ni$_3$(TAA)$_3$ (*P* = 34, 40, 55, 63, and 72%) are 291, 277, 141, 132, and 104 m^2 g^{-1}, respectively. These values are much lower than that of Ni$_3$(HITP)$_2$ (576 m^2 g^{-1}). The decreasing trend of the BET surface area in a series of *P*-Ni$_3$(TAA)$_3$ is due to the channel collapse and the installed substituents in pores during PSM. This is also true for the CO$_2$ adsorption uptake of *P*-Ni$_3$(TAA)$_3$ at 296 K and 760 mmHg, Fig. S11.† In the present case, the collapsed porosities verified by gas sorption data are able to prevent the diffusion of TMP to react with bis(diimine) nickel subunits in N$_3$(HITP)$_2$, leading to the partial conversion of coordination linkages in the MOF.

Photocatalysis

Under the reported optimized photocatalytic conditions with Ni$_3$(HITP)$_2$ for 2.0 hours (for details, please see the ESI†),[60] the post-synthetic materials show an increased CO production rate from 34%-Ni$_3$(TAA)$_3$ (13 230 μmol g^{-1} h^{-1}) to 40%-Ni$_3$(TAA)$_3$ (22 720 μmol g^{-1} h^{-1}) in Fig. 2a and Table S1,† followed by continuously decreasing rates of 17 820, 11 830, and 10 310 μmol g^{-1} h^{-1} for 55%-Ni$_3$(TAA)$_3$, 63%-Ni$_3$(TAA)$_3$, and 72%-Ni$_3$(TAA)$_3$, respectively. This might be caused by the decreased porosity after PSM from 12 to 18, 24, and 30 hours. Meanwhile, the low H$_2$ production rates in the range of 1460–980 μmol g^{-1} h^{-1} were disclosed for the *P*-Ni$_3$(TAA)$_3$ series, Fig. 2a and Table S1.† As a result, these photocatalysts have the highest CO/H$_2$ selectivity of 96% for 40%-Ni$_3$(TAA)$_3$, Table S1.† Obviously, the photocatalytic CO production rate for 40%-Ni$_3$(TAA)$_3$ is superior to that of Ni$_3$(HITP)$_2$ (13 230 μmol g^{-1} h^{-1}) possibly due to the improvement of electronic structures and catalytic sites after PSM. It is worth noting that the photocatalytic performance of 40%-Ni$_3$(TAA)$_3$ with both high CO generation rate and selectivity is better than many outstanding systems such as HOF-25-Re,[61] Ru@Cu-HHTP,[62]
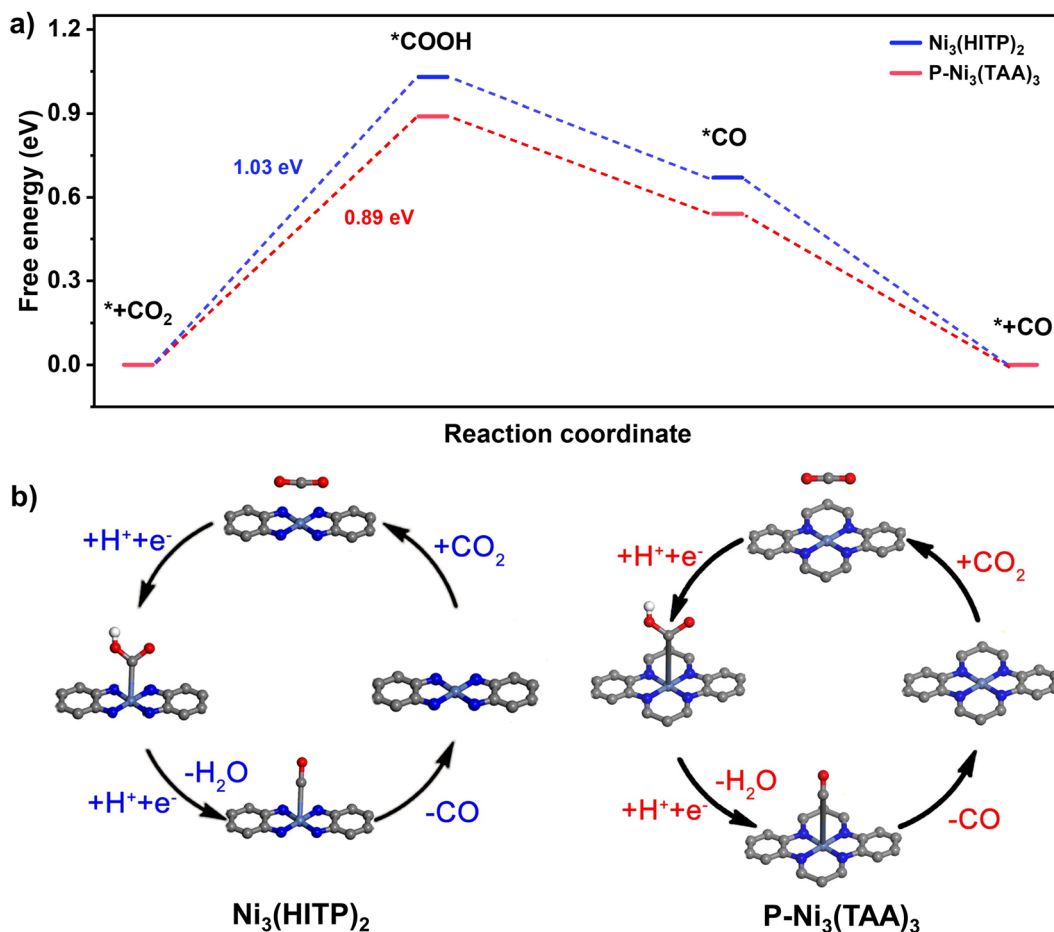
Fig. 3 (a) Free-energy diagrams of CO$_2$ reduction to CO for Ni$_3$(HITP)$_2$ and *P*-Ni$_3$(TAA)$_3$ (with 100% converted TAA metallomacrocycles). (b) A proposed reaction pathway for photocatalytic CO$_2$-to-CO conversion around a single metal site over Ni$_3$(HITP)$_2$ and 100%-Ni$_3$(TAA)$_3$.

4780 | *Inorg. Chem. Front.*, 2022, **9**, 4776–4784

This journal is © the Partner Organisations 2022

UrFe,[63] Ni(OH)$_2$-10%GR[64] and Ni@Ru-UiO-67,[65] Table S1.†
The present photocatalytic conversion from CO_2 to CO for
40%-Ni$_3$(TAA)$_3$ is further supported by various control experiments with either none or trace CO production and isotope labeling experiments, Fig. 2d and S19.† Five-cycle cycling measurements revealed a constant CO evolution rate above 21 420 μmol g^{-1} h^{-1} and 96% selectivity, Fig. 2c. The retention of crystallinity for 40%-Ni$_3$(TAA)$_3$ was demonstrated by SEM images and PXRD patterns, Fig. S20 and S21,† indicating its good photocatalytic stability. In addition, the control heterogeneous photocatalytic performances of mononuclear nickel compounds, 4HNi and Ni(TAA), are also determined under the same experimental conditions. The CO generation rate of 9400 μmol g^{-1} h^{-1} for Ni(TAA) is much higher than that of 4HNi (5700 μmol g^{-1} h^{-1}), Fig. 2a. The enhanced 65% photocatalytic CO reduction rate for Ni(TAA) compared to that of 4HNi is attributed to the higher activity of the former single metal site. This also gives additional support for the excellent photocatalytic performance of 40%-Ni$_3$(TAA)$_3$.

Structure–activity relationship

According to the UV-Vis diffuse reflectance spectra of Ni$_3$(HITP)$_2$ and 40%-Ni$_3$(TAA)$_3$, Fig. S14 and S18,† their similar band gaps (E_g) are determined to be 1.70 and 1.68 eV, respectively. Moreover, Mott–Schottky measurements of Ni$_3$(HITP)$_2$ and 40%-Ni$_3$(TAA)$_3$ at frequencies of 500, 1000, and 1500 Hz recognize their flat bands of −1.33 and −1.05 V, respectively, *vs.* Ag/AgCl. These values are ascribed to the energy levels of their LUMO bands. These results indicate the suitable electronic structures of Ni$_3$(HITP)$_2$ and 40%-Ni$_3$(TAA)$_3$ towards CO_2 reduction.[66] In addition, the theoretical simulation results disclose the quantitative free energy for CO_2RR intermediates. A four-step process has been calculated for Ni$_3$(HITP)$_2$ and 100%-Ni$_3$(TAA)$_3$, including CO_2 adsorption, *COOH formation, *CO production, and CO desorption,[67,68] Fig. 3b. Among the four steps, the generation of a *COOH intermediate with the highest free energy barrier is inferred as the potential determining step of the present CO_2 reduction reaction with Ni$_3$(HITP)$_2$ and 40%-Ni$_3$(TAA)$_3$ photocatalysts, Fig. 3a. The slightly lower value of the *COOH formation free energy barrier for 100%-Ni$_3$(TAA)$_3$ might be responsible for the higher photocatalytic performance of 40%-Ni$_3$(TAA)$_3$ in comparison with Ni$_3$(HITP)$_2$. It is worth noting that on the basis of the abovementioned experimental result, the porosity appears to also play an important role in the present CO_2 reduction photocatalysis.

4.   Conclusions

In summary, a post-synthetic strategy to form MOFs has been established towards fabricating metal-containing COFs. The chemical conversion of partial linkages and catalytic sites of the MOF has been realized and demonstrated, enabling the obvious enhancement of the solution resistance and photocatalytic activity of the resulting hemi-COF. This work not only introduces an interesting PSM approach of MOFs, but also indicates the existence of some balance between the catalytically active sites and porosity of post-synthetic reticular materials in their applications. The present result is believed to be helpful in investigations covering both MOFs and COFs.

Author contributions

Xinxin Wang, Ganggang Chang, Chenxi Liu, Ruidong Li, and Xiaolin Liu performed experiments under the guidance of Hailong Wang and Jianzhuang Jiang. Tianyu Wang, Yucheng Jin, and Xu Ding provided assistance for data acquisition and analysis. All authors discussed the results and commented on the manuscript.

Conflicts of interest

There are no conflicts to declare.

Acknowledgements

Notes and references

1 P. Q. Liao, N. Y. Huang, W. X. Zhang, J. P. Zhang and X. M. Chen, Controlling guest conformation for efficient purification of butadiene, *Science*, 2017, **356**, 1193–1196.

2 C. A. Trickett, A. Helal, B. A. Al-Maythalony, Z. H. Yamani, K. E. Cordova and O. M. Yaghi, The chemistry of metal–organic frameworks for CO_2 capture, regeneration and conversion, *Nat. Rev. Mater.*, 2017, **2**, 17045.

3 R.-B. Lin, Z. Zhang and B. Chen, chieving high performance metal–organic framework materials through pore engineering, *Acc. Chem. Res.*, 2021, **54**, 3362–3376.

4 T. Drake, P. Ji and W. Lin, Site isolation in metal–organic frameworks enables novel transition metal catalysis, *Acc. Chem. Res.*, 2018, **51**, 2129–2138.

5 S. Wan, J. Wu, D. Wang, H. Liu, Z. Zhang, J. Ma and C. Wang, Co/N-doped carbon nanotube arrays grown on 2D MOFs-derived matrix for boosting the oxygen reduction reaction in alkaline and acidic media, *Chin. Chem. Lett.*, 2021, **32**, 816–821.

6 X. Xiao, L. Zou, H. Pang and Q. Xu, Synthesis of micro/nanoscaled metal–organic frameworks and their direct electrochemical applications, *Chem. Soc. Rev.*, 2020, **49**, 301–331.

7 Y.-P. Xia, C.-X. Wang, M.-H. Yu and X.-H. Bu, A unique 3D microporous MOF constructed by cross-linking 1D coordi-

This journal is © the Partner Organisations 2022

Inorg. Chem. Front., 2022, **9**, 4776–4784 | **4781**

nation polymer chains for effectively selective separation of CO_2/CH_4 and C_2H_2/CH_4, *Chin. Chem. Lett.*, 2021, **32**, 1153–1156.

8 Y.-Z. Li, Z.-H. Fu and G. Xu, Metal-organic framework nanosheets: Preparation and applications, *Coord. Chem. Rev.*, 2019, **388**, 79–106.

9 Y. Cui, B. Li, H. He, W. Zhou, B. Chen and G. Qian, Metal–organic frameworks as platforms for functional materials, *Acc. Chem. Res.*, 2016, **49**, 483–493.

10 H. Zeng, M. Xie, T. Wang, R.-J. Wei, X.-J. Xie, Y. Zhao, W. Lu and D. Li, Orthogonal-array dynamic molecular sieving of propylene/propane mixtures, *Nature*, 2021, **595**, 542–548.

11 H. An, M. Li, J. Gao, Z. Zhang, S. Ma and Y. Chen, Incorporation of biomolecules in metal-organic frameworks for advanced applications, *Coord. Chem. Rev.*, 2019, **384**, 90–106.

12 S. Lin, C. S. Diercks, Y.-B. Zhang, N. Kornienko, E. M. Nichols, Y. Zhao, A. R. Paris, D. Kim, P. Yang, O. M. Yaghi and C. J. Chang, Covalent organic frameworks comprising cobalt porphyrins for catalytic CO_2 reduction in water, *Science*, 2015, **349**, 1208–1213.

13 X. Guan, F. Chen, Q. Fang and S. Qiu, Design and applications of three dimensional covalent organic frameworks, *Chem. Soc. Rev.*, 2020, **49**, 1357–1384.

14 K. Geng, T. He, R. Liu, S. Dalapati, K. T. Tan, Z. Li, S. Tao, Y. Gong, Q. Jiang and D. Jiang, Covalent organic frameworks: design, synthesis, and functions, *Chem. Rev.*, 2020, **120**, 8814–8933.

15 S.-Y. Ding and W. Wang, Covalent organic frameworks (COFs): from design to applications, *Chem. Soc. Rev.*, 2013, **42**, 548–568.

16 A. M. Evans, L. R. Parent, N. C. Flanders, R. P. Bisbey, E. Vitaku, M. S. Kirschner, R. D. Schaller, L. X. Chen, N. C. Gianneschi and W. R. Dichtel, Seeded growth of single-crystal two-dimensional covalent organic frameworks, *Science*, 2018, **361**, 52–57.

17 X. Han, C. Yuan, B. Hou, L. Liu, H. Li, Y. Liu and Y. Cui, Chiral covalent organic frameworks: design, synthesis and property, *Chem. Soc. Rev.*, 2020, **49**, 6248–6272.

18 Z. Wang, S. Zhang, Y. Chen, Z. Zhang and S. Ma, Covalent organic frameworks for separation applications, *Chem. Soc. Rev.*, 2020, **49**, 708–735.

19 L. Liu, L. Yin, D. Cheng, S. Zhao, H.-Y. Zang, N. Zhang and G. Zhu, Surface-mediated construction of an ultrathin free-standing covalent organic framework membrane for efficient proton conduction, *Angew. Chem., Int. Ed.*, 2021, **60**, 14875–14880.

20 J. Li, X. Jing, Q. Li, S. Li, X. Gao, X. Feng and B. Wang, Bulk COFs and COF nanosheets for electrochemical energy storage and conversion, *Chem. Soc. Rev.*, 2020, **49**, 3565–3604.

21 Y. Hu, L. J. Wayment, C. Haslam, X. Yang, S.-H. Lee, Y. Jin and W. Zhang, Covalent organic framework based lithium-ion battery: fundamental, design and characterization, *EnergyChem*, 2021, **3**, 100048.

22 Y. Jin, Y. Hu, M. Ortiz, S. Huang, Y. Ge and W. Zhang, Confined growth of ordered organic frameworks at an interface, *Chem. Soc. Rev.*, 2020, **49**, 4637–4666.

23 B. Gui, G. Lin, H. Ding, C. Gao, A. Mal and C. Wang, Three-dimensional covalent organic frameworks: from topology design to applications, *Acc. Chem. Res.*, 2020, **53**, 2225–2234.

24 H. Fang, B. Zheng, Z.-H. Zhang, H.-X. Li, D.-X. Xue and J. Bai, Ligand-conformer-induced formation of zirconium–organic framework for methane storage and MTO product separation, *Angew. Chem., Int. Ed.*, 2021, **60**, 16521–16528.

25 L. Li, R.-B. Lin, R. Krishna, H. Li, S. Xiang, H. Wu, J. Li, W. Zhou and B. Chen, Ethane/ethylene separation in a metal-organic framework with iron-peroxo sites, *Science*, 2018, **362**, 443–446.

26 J. Pei, X.-W. Gu, C.-C. Liang, B. Chen, B. Li and G. Qian, Robust and radiation-resistant hofmann-type metal–organic frameworks for record xenon/krypton separation, *J. Am. Chem. Soc.*, 2022, **144**, 3200–3209.

27 W. Fan, X. Zhang, Z. Kang, X. Liu and D. Sun, Isoreticular chemistry within metal–organic frameworks for gas storage and separation, *Coord. Chem. Rev.*, 2021, **443**, 213968.

28 Y. Wang, L. Yan, K. Dastafkan, C. Zhao, X. Zhao, Y. Xue, J. Huo, S. Li and Q. Zhai, Lattice matching growth of conductive hierarchical porous MOF/LDH heteronanotube arrays for highly efficient water oxidation, *Adv. Mater.*, 2021, **33**, 2006351.

29 J. Guo, Y. Qin, Y. Zhu, X. Zhang, C. Long, M. Zhao and Z. Tang, Metal–organic frameworks as catalytic selectivity regulators for organic transformations, *Chem. Soc. Rev.*, 2021, **50**, 5366–5396.

30 X.-L. Lv, K. Wang, B. Wang, J. Su, X. Zou, Y. Xie, J.-R. Li and H.-C. Zhou, A base-resistant metalloporphyrin metal–organic framework for C–H bond halogenation, *J. Am. Chem. Soc.*, 2017, **139**, 211–217.

31 J.-D. Yi, D.-H. Si, R. Xie, Q. Yin, M.-D. Zhang, Q. Wu, G.-L. Chai, Y.-B. Huang and R. Cao, Conductive two-dimensional phthalocyanine-based metal–organic framework nanosheets for efficient electroreduction of CO_2, *Angew. Chem., Int. Ed.*, 2021, **60**, 17108–17114.

32 Y. Wen, J. Zhang, Q. Xu, X.-T. Wu and Q.-L. Zhu, Pore surface engineering of metal–organic frameworks for heterogeneous catalysis, *Coord. Chem. Rev.*, 2018, **376**, 248–276.

33 H.-Y. Li, S.-N. Zhao, S.-Q. Zang and J. Li, Functional metal–organic frameworks as effective sensors of gases and volatile compounds, *Chem. Soc. Rev.*, 2020, **49**, 6364–6401.

34 T.-Y. Luo, P. Das, D. L. White, C. Liu, A. Star and N. L. Rosi, Luminescence "turn-on" detection of gossypol using Ln^{3+}-based metal–organic frameworks and Ln^{3+} salts, *J. Am. Chem. Soc.*, 2020, **142**, 2897–2904.

35 J. Dong, X. Han, Y. Liu, H. Li and Y. Cui, Metal–covalent organic frameworks (MCOFs): a bridge between metal–organic frameworks and covalent organic frameworks, *Angew. Chem., Int. Ed.*, 2020, **59**, 13722–13733.

4782 | *Inorg. Chem. Front.*, 2022, **9**, 4776–4784

This journal is © the Partner Organisations 2022

36 X. Feng, Y. Ren and H. Jiang, Metal-bipyridine/phenanthro-line-functionalized porous crystalline materials: Synthesis and catalysis, *Coord. Chem. Rev.*, 2021, **438**, 213907.

37 M. Chen, H. Li, C. Liu, J. Liu, Y. Feng, A. G. H. Wee and B. Zhang, Porphyrin- and porphyrinoid-based covalent organic frameworks (COFs): From design, synthesis to applications, *Coord. Chem. Rev.*, 2021, **435**, 213778.

38 H.-Y. Wu, Y.-Y. Qin, Y.-H. Xiao, J.-S. Chen, R. Guo, S.-Q. Wu, L. Zhang, J. Zhang and Y.-G. Yao, Synergistic Lewis acid and Pd active sites of metal–organic frameworks for highly efficient carbonylation of methyl nitrite to dimethyl carbonate, *Inorg. Chem. Front.*, 2022, **9**, 2379–2388.

39 B. Han, Y. Jin, B. Chen, W. Zhou, B. Yu, C. Wei, H. Wang, K. Wang, Y. Chen, B. Chen and J. Jiang, Maximizing elec-troactive sites in a three-dimensional covalent organic framework for significantly improved carbon dioxide reduction electrocatalysis, *Angew. Chem.*, 2022, **61**, e202114244.

40 L.-H. Li, X.-L. Feng, X.-H. Cui, Y.-X. Ma, S.-Y. Ding and W. Wang, Salen-based covalent organic framework, *J. Am. Chem. Soc.*, 2017, **139**, 6042–6045.

41 Y. Meng, Y. Luo, J.-L. Shi, H. Ding, X. Lang, W. Chen, A. Zheng, J. Sun and C. Wang, 2D and 3D porphyrinic covalent organic frameworks: the influence of dimensional-ity on functionality, *Angew. Chem., Int. Ed.*, 2020, **59**, 3624–3629.

42 Y. Qian, D. Li, Y. Han and H.-L. Jiang, Photocatalytic mole-cular oxygen activation by regulating excitonic effects in covalent organic frameworks, *J. Am. Chem. Soc.*, 2020, **142**, 20763–20771.

43 M. Wang, M. Ballabio, M. Wang, H.-H. Lin, B. P. Biswal, X. Han, S. Paasch, E. Brunner, P. Liu, M. Chen, M. Bonn, T. Heine, S. Zhou, E. Cánovas, R. Dong and X. Feng, Unveiling electronic properties in metal–phthalocyanine-based pyrazine-linked conjugated two-dimensional covalent organic frameworks, *J. Am. Chem. Soc.*, 2019, **141**, 16810–16816.

44 H.-S. Lu, W.-K. Han, X. Yan, C.-J. Chen, T. Niu and Z.-G. Gu, A 3D anionic metal covalent organic framework with soc topology built from an octahedral Ti^{IV} complex for photocatalytic reactions, *Angew. Chem., Int. Ed.*, 2021, **60**, 17881–17886.

45 X. Kang, X. Han, C. Yuan, C. Cheng, Y. Liu and Y. Cui, Reticular synthesis of tbo topology covalent organic frame-works, *J. Am. Chem. Soc.*, 2020, **142**, 16346–16356.

46 L. Sun, M. Lu, Z. Yang, Z. Yu, X. Su, Y.-Q. Lan and L. Chen, Nickel glyoximate based metal–covalent organic frame-works for efficient photocatalytic hydrogen evolution, *Angew. Chem., Int. Ed.*, 2022, e202204326.

47 Q. Guan, L.-L. Zhou and Y.-B. Dong, Metalated covalent organic frameworks: from synthetic strategies to diverse applications, *Chem. Soc. Rev.*, 2022, DOI: **10.1039/ D1CS00983D**.

48 S. Chen, P. Kong, H. Niu, H. Liu, X. Wang, J. Zhang, R. Li, Y. Guo and T. Peng, Co-porphyrin/Ru-pincer complex

coupled polymer with Z-scheme molecular junctions and dual single-atom sites for visible light-responsive CO_2 reduction, *Chem. Eng. J.*, 2022, **431**, 133357.

49 J. Han, N. Li, D. Chen, Q. Xu and J. Lu, Boosting photo-catalytic activity for porphyrin-based D-A conjugated polymers via dual metallic sites regulation, *Appl. Catal., B*, 2022, **317**, 121724.

50 S. M. Cohen, Postsynthetic methods for the functionali-zation of metal–organic frameworks, *Chem. Rev.*, 2012, **112**, 970–1000.

51 J. H. Kim, D. W. Kang, H. Yun, M. Kang, N. Singh, J. S. Kim and C. S. Hong, Post-synthetic modifications in porous organic polymers for biomedical and related applications, *Chem. Soc. Rev.*, 2022, **51**, 43–56.

52 Y. Wang, J.-P. Chang, R. Xu, S. Bai, D. Wang, G.-P. Yang, L.-Y. Sun, P. Li and Y.-F. Han, N-Heterocyclic carbenes and their precursors in functionalised porous materials, *Chem. Soc. Rev.*, 2021, **50**, 13559–13586.

53 S. M. Cohen, The postsynthetic renaissance in porous solids, *J. Am. Chem. Soc.*, 2017, **139**, 2855–2863.

54 A. L. Balchla and R. H. HoImlb, Complete electron-transfer series of the [M-N$_4$] type, *J. Am. Chem. Soc.*, 1996, 88.

55 D. Sheberla, L. Sun, M. A. Blood-Forsythe, S. Er, C. R. Wade, C. K. Brozek, A. Aspuru-Guzik and M. Dincă, High electrical conductivity in Ni$_3$(2,3,6,7,10,11-hexaiminotriphenylene)$_2$, a semiconducting metal–organic graphene analogue, *J. Am. Chem. Soc.*, 2014, **136**, 8859–8862.

56 T. Chen, J.-H. Dou, L. Yang, C. Sun, N. J. Libretto, G. Skorupskii, J. T. Miller and M. Dincă, Continuous electrical conductivity variation in M$_3$(Hexaiminotriphenylene)$_2$ (M = Co, Ni, Cu) MOF alloys, *J. Am. Chem. Soc.*, 2020, **142**, 12367–12373.

57 Y. Jiang, I. Oh, S. H. Joo, O. Buyukcakir, X. Chen, S. H. Lee, M. Huang, W. K. Seong, S. K. Kwak, J.-W. Yoo and R. S. Ruoff, Partial oxidation-induced electrical conductivity and paramagnetism in a Ni(II) tetraaza[14]annulene-linked metal organic framework, *J. Am. Chem. Soc.*, 2019, **141**, 16884–16893.

58 Y. Yue, P. Cai, X. Xu, H. Li, H. Chen, H.-C. Zhou and N. Huang, Conductive metallophthalocyanine framework films with high carrier mobility as efficient chemiresistors, *Angew. Chem., Int. Ed.*, 2021, **60**, 10806–10813.

59 Y. Lian, W. Yang, C. Zhang, H. Sun, Z. Deng, W. Xu, L. Song, Z. Ouyang, Z. Wang, J. Guo and Y. Peng, Unpaired 3d electrons on atomically dispersed cobalt centres in coordination polymers regulate both oxygen reduction reac-tion (ORR) activity and selectivity for use in zinc–air bat-teries, *Angew. Chem., Int. Ed.*, 2020, **59**, 286–294.

60 W. Zhu, C. Zhang, Q. Li, L. Xiong, R. Chen, X. Wan, Z. Wang, W. Chen, Z. Deng and Y. Peng, Selective reduction of CO_2 by conductive MOF nanosheets as an efficient co-catalyst under visible light illumination, *Appl. Catal., B*, 2018, **238**, 339–345.

61 B. Yu, L. Li, S. Liu, H. Wang, H. Liu, C. Lin, C. Liu, H. Wu, W. Zhou, X. Li, T. Wang, B. Chen and J. Jiang, Robust bio-

This journal is © the Partner Organisations 2022

Inorg. Chem. Front., 2022, **9**, 4776–4784 | **4783**

logical hydrogen-bonded organic framework with post-functionalized rhenium(I) sites for efficient heterogeneous visible-light-driven CO_2 reduction, *Angew. Chem., Int. Ed.*, 2021, **60**, 8983–8989.

62 N.-Y. Huang, H. He, S. Liu, H.-L. Zhu, Y.-J. Li, J. Xu, J.-R. Huang, X. Wang, P.-Q. Liao and X.-M. Chen, Electrostatic attraction-driven assembly of a metal–organic framework with a photosensitizer boosts photocatalytic CO_2 reduction to CO, *J. Am. Chem. Soc.*, 2021, **143**, 17424–17430.

63 E. Pugliese, P. Gotico, I. Wehrung, B. Boitrel, A. Quaranta, M.-H. Ha-Thi, T. Pino, M. Sircoglou, W. Leibl, Z. Halime and A. Aukauloo, Dissection of light-induced charge accumulation at a highly active iron porphyrin: insights in the photocatalytic CO2 reduction, *Angew. Chem.*, 2022, **61**, e202202924.

64 K.-Q. Lu, Y.-H. Li, F. Zhang, M.-Y. Qi, X. Chen, Z.-R. Tang, Y. M. A. Yamada, M. Anpo, M. Conte and Y.-J. Xu, Rationally designed transition metal hydroxide nanosheet arrays on graphene for artificial CO_2 reduction, *Nat. Commun.*, 2020, **11**, 5181.

65 Z.-H. Yan, B. Ma, S.-R. Li, J. Liu, R. Chen, M.-H. Du, S. Jin, G.-L. Zhuang, L.-S. Long, X.-J. Kong and L.-S. Zheng, Encapsulating a Ni(II) molecular catalyst in photoactive metal–organic framework for highly efficient photoreduction of CO_2, *Sci. Bull.*, 2019, **64**, 976–985.

66 M. Lu, J. Liu, Q. Li, M. Zhang, M. Liu, J.-L. Wang, D.-Q. Yuan and Y.-Q. Lan, Rational design of crystalline covalent organic frameworks for efficient CO_2 photoreduction with H_2O, *Angew. Chem., Int. Ed.*, 2019, **58**, 12392–12397.

67 Y. Hu, F. Zhan, Q. Wang, Y. Sun, C. Yu, X. Zhao, H. Wang, R. Long, G. Zhang, C. Gao, W. Zhang, J. Jiang, Y. Tao and Y. Xiong, Tracking mechanistic pathway of photocatalytic CO_2 reaction at Ni sites using operando, time-resolved spectroscopy, *J. Am. Chem. Soc.*, 2020, **142**, 5618–5626.

68 Q. Liu, Q. Wang, J. Wang, Z. Li, J. Liu, X. Sun, J. Li, Y. Lei, L. Dai and P. Wang, TpyCo^{2+}-based coordination polymers by water-induced gelling trigged efficient oxygen evolution reaction, *Adv. Funct. Mater.*, 2020, **30**, 2000593.